5

NA source inversion II - application to observed data

5.1 Introduction

In the previous chapter we have shown that the NA approach works extremely well with synthetic input data, even in the presence of noise. The purpose of this chapter is to illustrate that the NA source inversion also works well with real data, but that there are occasionally circumstances in which we are unable to achieve a satisfactory fit to the observed seismograms. We illustrate the performance of the inversion for six events with moderate magnitudes, and a range of source depths. Five of the events have CMT solutions published by Harvard University, which provides an estimate of the source depth and mechanism with which we can compare our inversion results. As a test of the discrimination capabilities of the NA inversion, we also perform inversion for a known nuclear explosion, treating it in a similar way to the other events.

The first event occurred off the east coast of Honshu, Japan. Since this event is located beneath the ocean, it is necessary to perform an adaptive inversion allowing for an oceanic layer above the source. Inversion using a standard velocity model works well for the second event which occurred in southern Xinjiang, China, since it is located in a continental region. We also illustrate inversion with complex synthetic seismograms for this event. The effects of using different misfit measures with real data is investigated for the southern Xinjiang event. We also use this event as an example to illustrate the range of models which satisfactorily fit the data. The third event occurred in Kyrgyzstan, and again we obtain good results using a standard velocity model since the earthquake occurred in a continental region. We also perform inversion for an Indian nuclear explosion, and obtain a very shallow depth estimate, as well as a large isotropic component estimate, providing strong evidence that the event was a nuclear test. The fifth event which we consider occurred in Turkey.

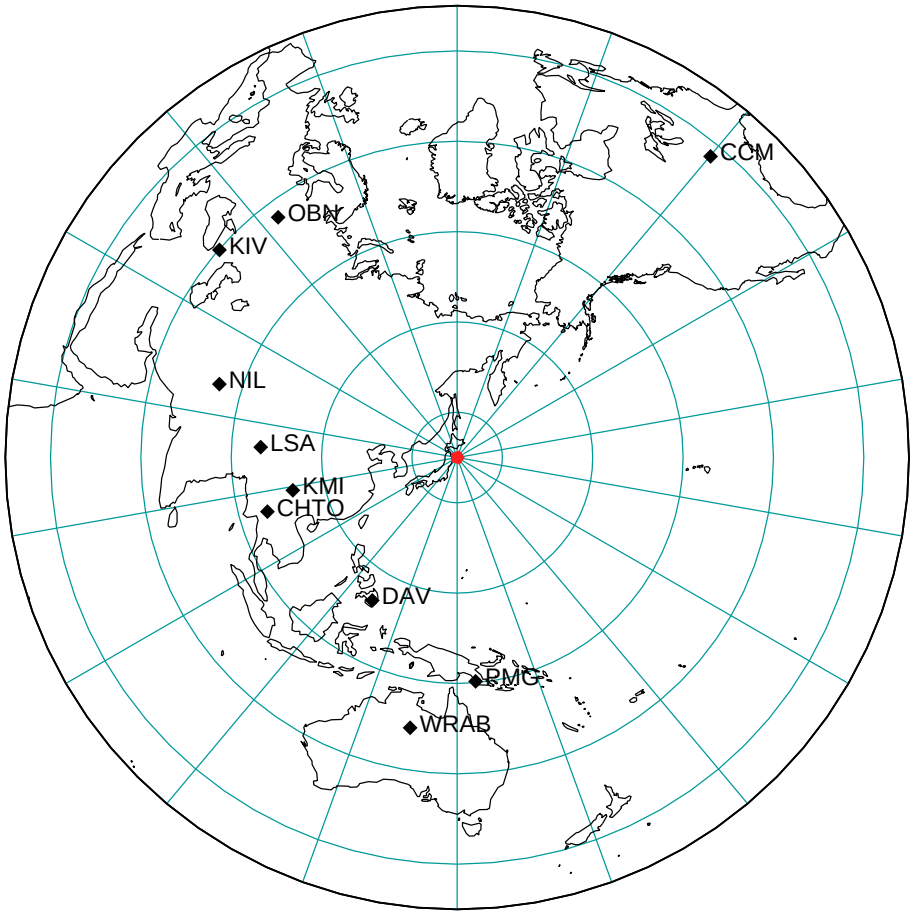

Fig. 5.1. Location of the 14 May 1998 Honshu event along with the station distribution used in the inversion.

Unfortunately we are unable to constrain the source mechanism due to poor azimuthal coverage relative to the source radiation pattern, however we obtain a reasonable depth estimate. We are unable to obtain a satisfactory seismogram fit for the sixth event which occurred on the India-Bangladesh border. The presence of strong crustal heterogeneity in the vicinity of this event means that our simple modelling scheme is unable to obtain a reliable inversion result.

5.2 Honshu event

For our first illustration of source mechanism and depth inversion with observed data, we use an event which occurred off the east coast of Honshu, Japan (Figure 5.1) on 14 May 1998. This event has an estimated m_b of 5.8, so is large enough to have a CMT solution (Dziewonski et al., 1999b), providing a model with which we can compare our inversion results. The estimated depth from the CMT solution is 19 km.

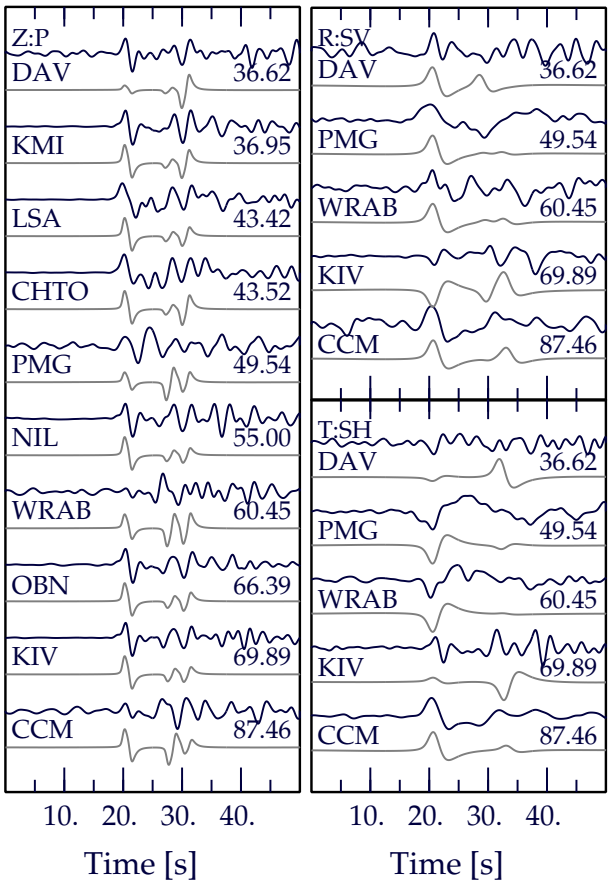

Fig. 5.2. Comparison between the observed (black traces) and predicted (grey traces) seismograms for the Honshu event with the standard *ak135* velocity model. Shown are the vertical component of *P*, and the radial and transverse components of *S*. Each set of traces is annotated with the station name and epicentral distance.

The waveforms have been obtained from the Incorporated Research Institutions for Seismology Data Management Centre (IRIS DMC). Ten stations are used in the inversion, however only five of the stations have suitable *SV* and *SH* waveforms due to low signal to *P* coda ratios for *S*. A weighting factor is therefore applied to the *S* wave data in order to account for this. The waveforms are bandpass filtered in the range 0.01 Hz to 0.6 Hz before inversion. Both the observed and synthetic data are normalised to unit maximum amplitude prior to inversion, so that factors such as the scalar moment do not need to be included.

5.2.1 Standard inversion

Initially the inversion is performed in the standard way, using the *ak135* velocity model and a moment tensor representation of the source mechanism. A wide range

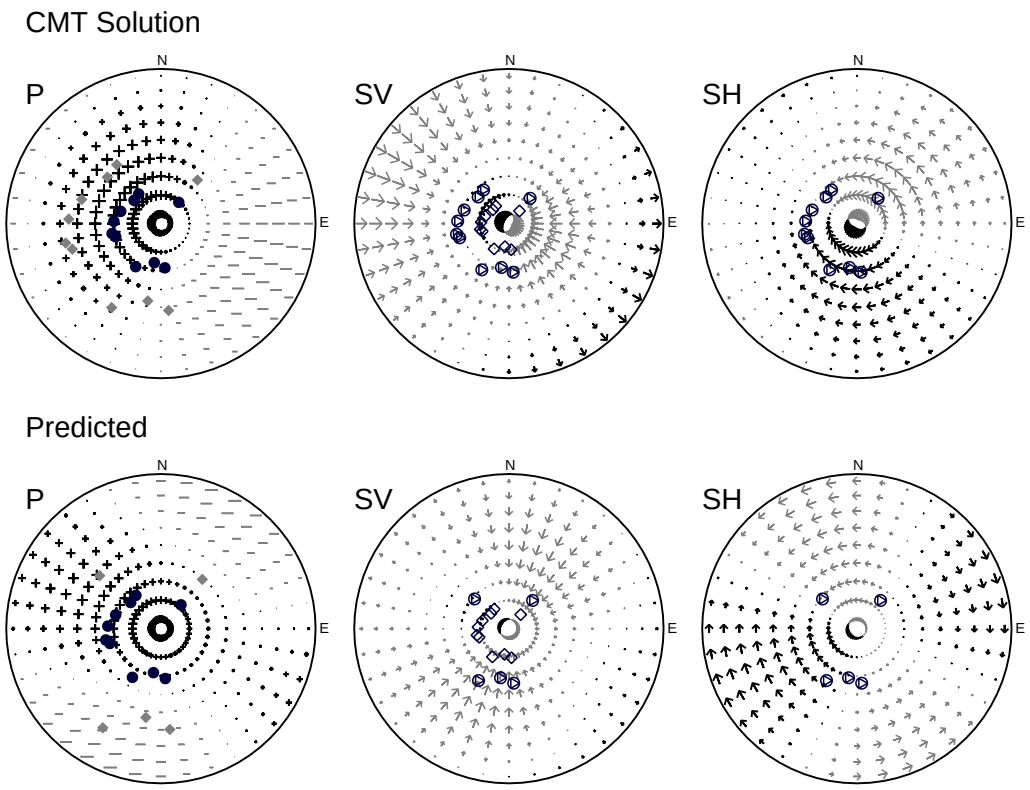

Fig. 5.3. Source radiation patterns for *P*, *SV* and *SH* waves for the Honshu event, using the CMT solution (top), and the predicted source mechanism obtained from inversion with the standard *ak135* velocity model (bottom). The plotted symbols represent the average take-off angle and azimuth for various phases; solid circles for *P*, solid triangles for *pP*, solid (grey) diamonds for *pS*; open circles for *S*, open triangles for *sS*, and open diamonds for *sP*.

of source depths, from 5 km to 40 km, are searched in the inversion. The first set of inversions reveal that the resulting synthetics are not matching the observed seismograms very well (Figure 5.2), and the source mechanism differs significantly from the CMT solution (Figure 5.3). Further tests with more complicated source time functions were performed, to see if the simple parameterisation being used is adequately modelling the observed seismograms. Firstly, an additional parameter was introduced, so that two source time function parameters are included in the inversion; the rise time of the trapezoid and the time length of the constant portion. This did not significantly improve the seismogram fit. A more complicated source time function was then introduced in the form of the superposition of two triangles, so that two rise time parameters are included in the inversion. Again, this did not improve the seismogram fit. The source depth estimates obtained from the various inversions are all around 22 km, which is close to the CMT depth of 19 km.

5.2.2 Adaptive inversion

Since this event occurred beneath the ocean, our inability to achieve a satisfactory seismogram fit using the standard *ak135* velocity model is not really surprising. This indicates that it is necessary to allow for an improved representation of the structure above the source when performing inversion for sub-oceanic events. This can easily be achieved, since we are using a derivative-free inversion scheme with an allowance for different structures at the source and receiver ends. We adapt the *ak135* velocity model to include a water layer above the source, and calculate additional phases such as *pwP, swP, swS, pwS* in order to take into account reflections off the water interface as well as off the seabed interface. Water depths in the range 1 to 2 km were tested, and a water depth of 1.25 km was found to give the best fit. A *P*-wave velocity of 1.5 km/s is used, with a density of 1.03 g/cm^3, for the water layer. The inversion is performed using *P, SV* and *SH* waveforms, and a moment tensor representation of the source mechanism is used. Again a wide range of source depths, from 5 km to 40 km, are searched in the inversion.

A significant improvement in the fit between the observed and synthetic seismograms is obtained when a water layer above the source is included (Figure 5.4). Note that the *P* waveforms at the stations WRAB and CCM (which have small *P* arrivals) are fit very poorly using the standard *ak135* model, however, with the inclusion of a water layer above the source the waveform fit at these two stations is greatly improved. The relative amplitudes at the station WRAB are not fit very well, but the relative timing and overall pulse shape are. Station PMG is fit poorly, even when taking into account the sub-oceanic source, and the likely explanation is the presence of sedimentary layers near the receiver, causing large amplitude reverberations after the initial *P* arrival. Such effects are not modelled in the inversion.

The recovered source mechanism is a good representation of the mechanism obtained from the CMT inversion (Figure 5.5). This is encouraging given the limited sampling of the source radiation pattern due to the small number of stations and rather poor azimuthal coverage. The recovered source depth is 18 km, which is shallower than that obtained with the standard *ak135* model and is in fact closer to the CMT depth of 19 km. A source depth of 18 km provides a better fit to the observed seismograms, and in particular the *S* waveforms. The two depth estimates obtained from the standard and adaptive inversions differ by only 4 km, which illustrates that a reasonably well constrained source depth can be obtained, even when the use of a standard velocity model such as *ak135* is not a good representation of the true structure.

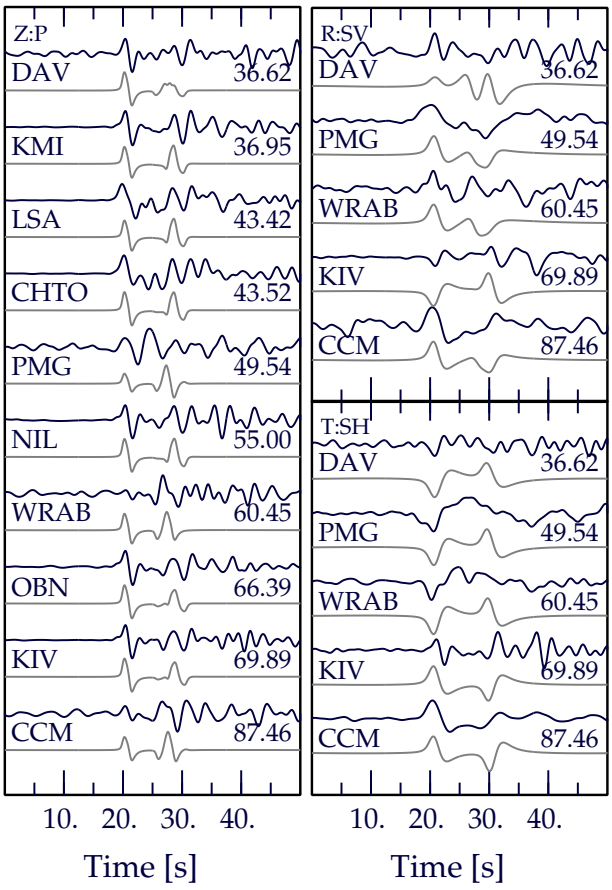

Fig. 5.4. Comparison between the observed (black traces) and predicted (grey traces) seismograms for the Honshu event with the inclusion of a water layer above the source. Shown are the vertical component of *P*, and the radial and transverse components of *S*. Each set of traces is annotated with the station name and epicentral distance.

There are other factors which are not modelled, which could explain discrepancies in the seismogram fit. Firstly, the earthquake occurred within a subduction zone, therefore the effect of dipping structure could be important. Our synthetics are calculated assuming a horizontally stratified medium. Near source structure is likely to have influenced the waveforms at WRAB, PMG and CCM, since the propagation paths to these stations start out along the strike of subduction zones; the Honshu and Izu-Bonin zones for WRAB and PMG, and the Kuril zone for CCM. There is also a 1 to 2 km thick sedimentary layer beneath the ocean off the Pacific coast of northern Honshu, as revealed by a seismic refraction study (Asano et al., 1981). In a study of earthquakes along the northern Honshu arc, Seno and Kroeger (1983) found that it was necessary to include this sedimentary layer, because the reflection from the bottom of the sediment is very large. Perhaps this can explain some of the arrivals seen between

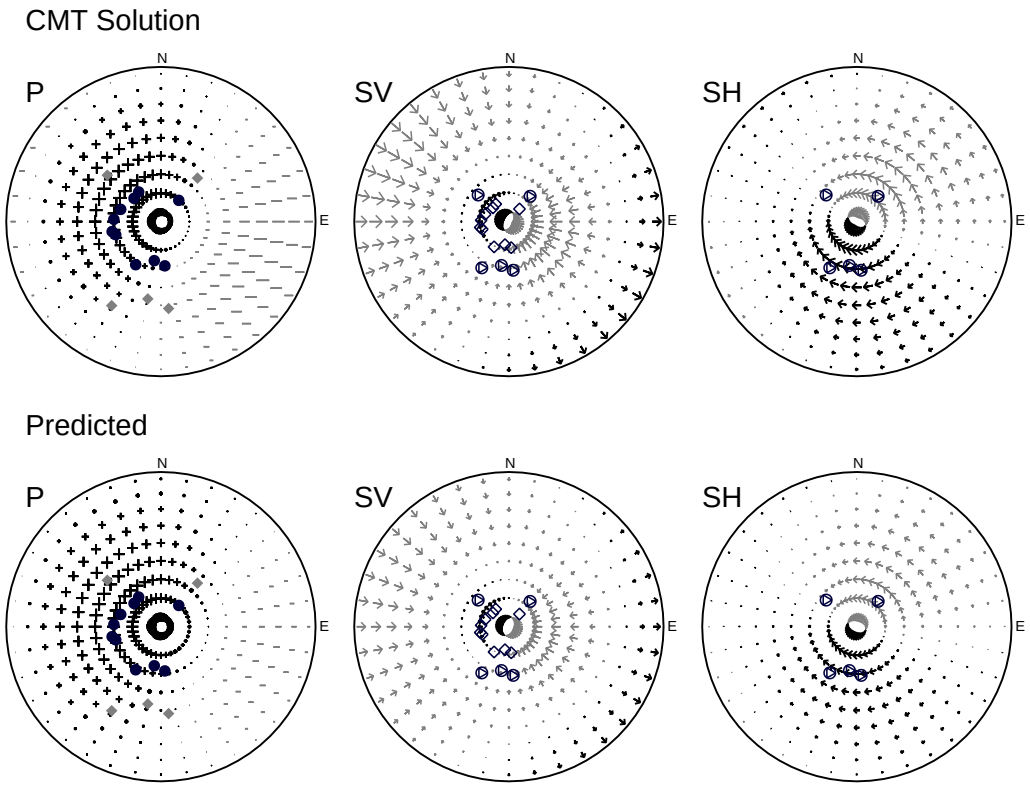

Fig. 5.5. Source radiation patterns for *P*, *SV* and *SH* waves for the Honshu event, using the CMT solution (top), and the predicted source mechanism obtained from inversion with a water layer above the source (bottom). The plotted symbols represent the average take-off angle and azimuth for various phases; solid circles for *P*, solid triangles for *pP*, solid (grey) diamonds for *pS*; open circles for *S*, open triangles for *sS*, and open diamonds for *sP*.

P and *pP*, which are not being fit. There also seems to be evidence for significant differences in *S* wave attenuation along the paths to different stations, which could be contributing to the fairly poor fit between the observed and synthetic *S* waveforms.

5.3 Southern Xinjiang event

The event used as our second illustration occurred in the continental region of southern Xinjiang, China (Figure 5.6) on 6 April 1997. This event has an estimated m_b of 5.6, with a CMT depth estimate of 15 km. Thus we can again compare our inversion results with the CMT solution for this event (Dziewonski et al., 1999a). A depth estimate of less than 15 km is acceptable, since it is well known that the CMT method cannot resolve depths shallower than 15 km (Dziewonski et al., 1987). The waveforms used in the inversion have been obtained from the IRIS DMC. Again, ten stations are used in the inversion, but only five of the stations have suitable *SV* and

Fig. 5.6. Location of the 6 April 1997 southern Xinjiang event along with the station distribution used in the inversion.

SH waveforms due to low signal to *P* coda ratios for *S*. The waveforms are bandpass filtered in the range 0.01 Hz to 0.7 Hz before inversion.

5.3.1 Standard inversion

Inversion with the standard *ak135* velocity model works well in this case, since the earthquake occurred in a continental region. We perform a joint *P* and *S* inversion, with a suitable weighting factor applied to the *S* wave data due to differing amounts of *P* and *S* information available. A wide range of source depths, from 0 km to 35 km, are searched in the inversion, and a moment tensor representation of the source mechanism is used. A significant isotropic (implosive) component is obtained, with a normalised moment tensor trace of -1.1. This isotropic estimate is not really surprising given the sampling distribution of the *P* radiation pattern (see Figure 5.8). Even though a significant isotropic component is recovered the seismogram fit is good.

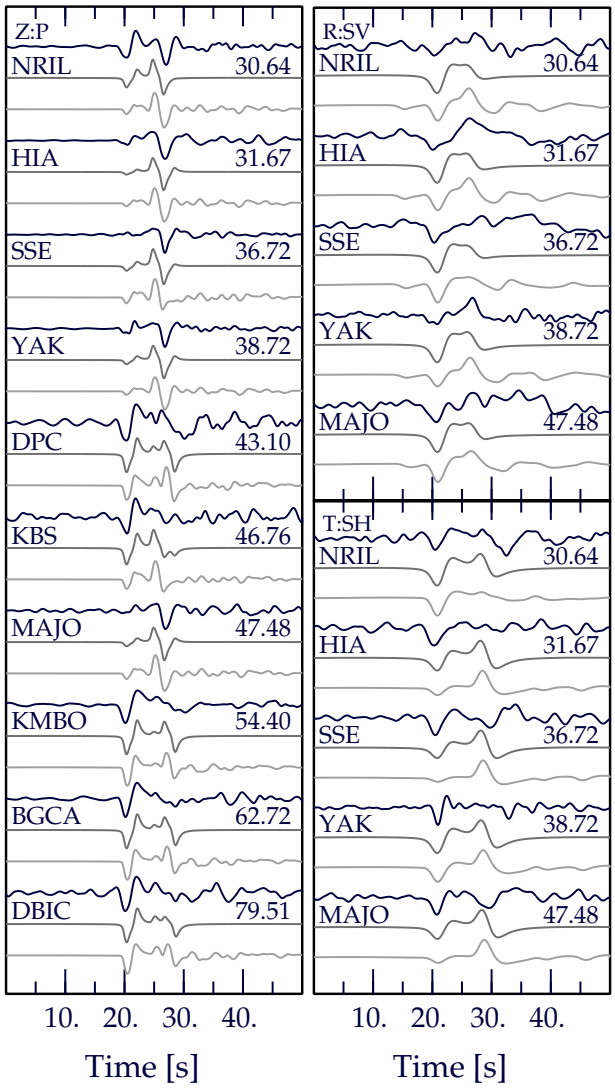

Fig. 5.7. Comparison between seismograms for the southern Xinjiang event: observed seismograms (black traces) along with predicted seismograms using simple synthetics (grey traces) and more complex synthetics (light grey traces). Shown are the vertical component of *P*, and the radial and transverse components of *S*. Each set of traces is annotated with the station name and epicentral distance.

The isotropic component is then constrained to be zero and the inversion is performed again. A good fit is achieved for the *P* and *SV* wave seismograms, but not for the *SH* seismograms. It seems that an introduced isotropic component may be compensating for deficiencies in the modelling, such as the use of a standard velocity model. Thus, when a constrained inversion is performed, it may be best to apply a non-zero constraint, and allow for a small, but not significant isotropic component. We therefore perform the inversion again, with the isotropic component constrained to have the value -0.1. An excellent fit is achieved for the *P* wave seismograms, and a reasonable

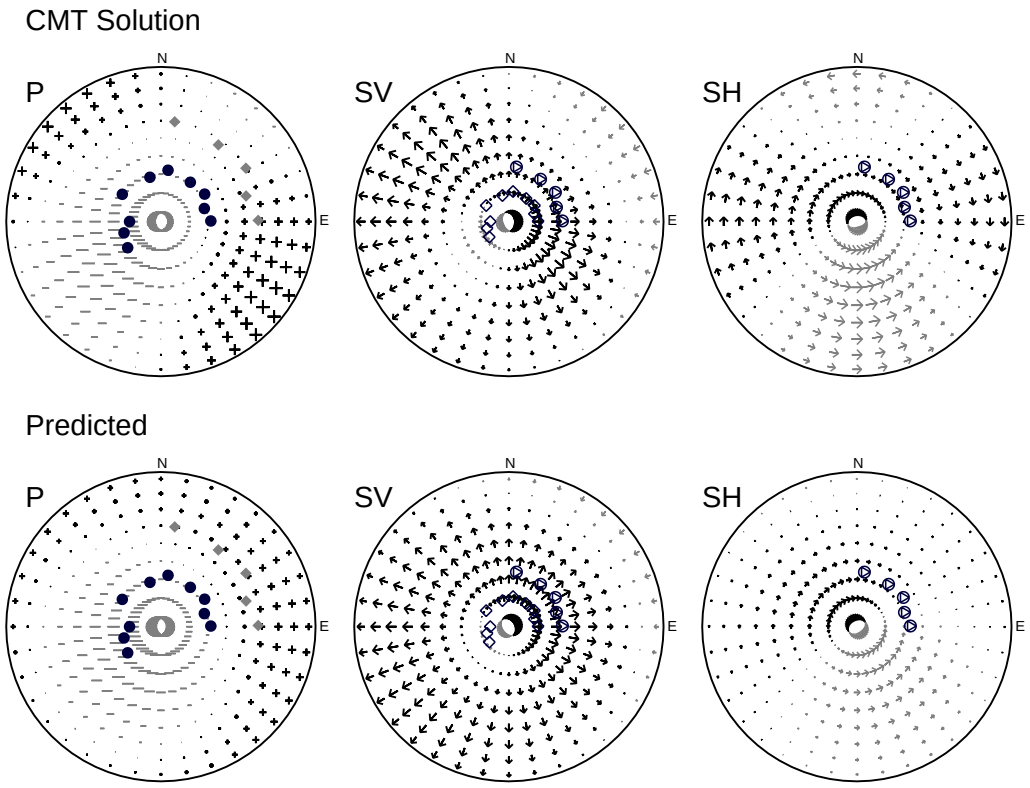

Fig. 5.8. Source radiation patterns for *P*, *SV* and *SH* waves for the southern Xinjiang event, using the CMT solution (top), and the predicted source mechanism obtained from the inversion (bottom). The plotted symbols represent the average take-off angle and azimuth for various phases; solid circles for *P*, solid triangles for *pP*, solid (grey) diamonds for *pS*; open circles for *S*, open triangles for *sS*, and open diamonds for *sP*.

fit is achieved for the *S* wave seismograms (Figure 5.7). The recovered source depth is 15 km, which is the same as the CMT estimate. We obtain good correspondence between the source mechanism estimate obtained from the NA inversion and the CMT inversion (Figure 5.8).

5.3.2 Flexible inversion

As an illustration of the flexibility of the NA inversion scheme we perform inversion with more complex synthetic seismograms which allow for the full suite of crustal reverberations and conversions at both the source and receiver ends (see Chapter 2). Since we are using a derivative-free inversion scheme it is easy to substitute a more complex modelling scheme into the inversion, however it does require significant computation time; around 3 hours on a Sun Sparc Ultra 5, compared to around 15 minutes for generalised ray theory. A comparison between the observed and predicted

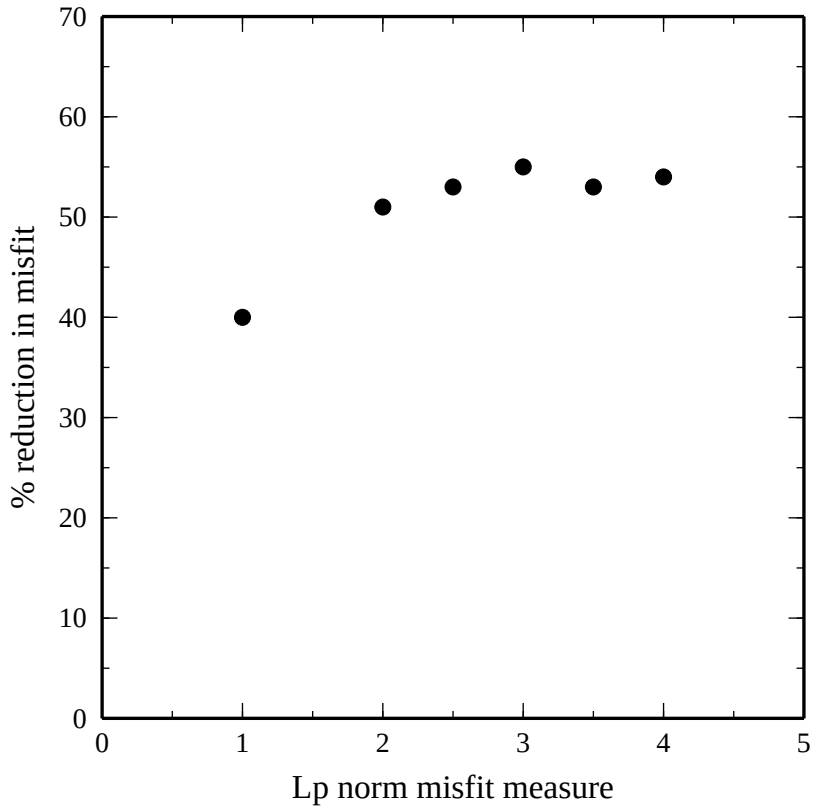

Fig. 5.9. Reduction in misfit (expressed as a percentage) for various L_p norm measures for the southern Xinjiang event.

seismograms for both the simple and complex synthetic computation schemes is shown in Figure 5.7. It can be seen that both calculation schemes produce similar looking predicted seismograms, though there are extra arrivals evident on the complex traces as would be expected. The use of the more complex synthetics in the inversion gives a depth estimate of 15 km, which is the same as that obtained using generalised ray theory. Similar estimates of the source mechanism are also obtained. This justifies the use of a simple generalised ray scheme in this case, however, it may be necessary to use more accurate synthetics for problematic events.

5.3.3 Comparison of misfit measures

Since we are using a derivative-free inversion scheme, based on only the rank of the misfit function, we can investigate the use of different misfit measures with real data. We have previously investigated L_p norm measures with $p = 1, 1.5, 2$ using synthetic data (Section 4.4). An advantage of the L_1 and $L_{1.5}$ measures over the conventional squared residual measure is that they are robust and tolerant to outliers. However,

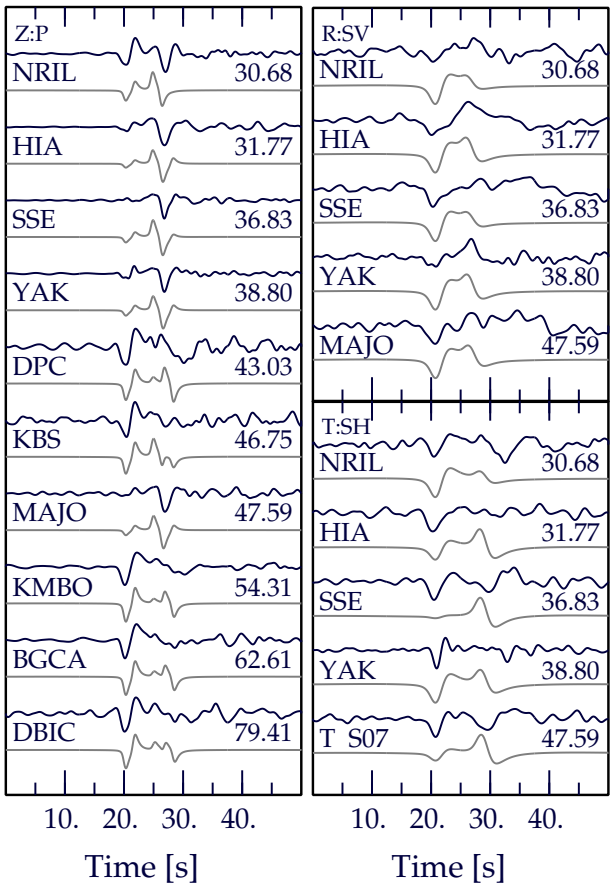

Fig. 5.10. Comparison between the observed (black traces) and predicted (grey traces) seismograms for the southern Xinjiang event using a L_3 norm. Shown are the vertical component of *P*, and the radial and transverse components of *S*. Each set of traces is annotated with the station name and epicentral distance.

tests with synthetic data have shown that the L_1 and $L_{1.5}$ norms do not provide strong enough constraints and tend to lead to local minima. Therefore, up until now, we have used a L_2 norm misfit measure in our inversions.

In light of these results we now investigate the use of L_p norm measures with $p > 2$ for the southern Xinjiang event. Such misfit measures are less tolerant to outliers and so should provide stronger constraints, however they may also be affected by noise. We investigate L_p norm measures with $p = 2.5, 3, 3.5, 4$, along with a L_1 norm measure for comparison. In order to compare the various misfit measures we calculate the reduction in misfit relative to the initial misfit value, expressed as a percentage. These results are displayed in Figure 5.9 for the various L_p norm measures that have been investigated. The use of a L_3 norm misfit measure gives the largest reduction in misfit for this event.

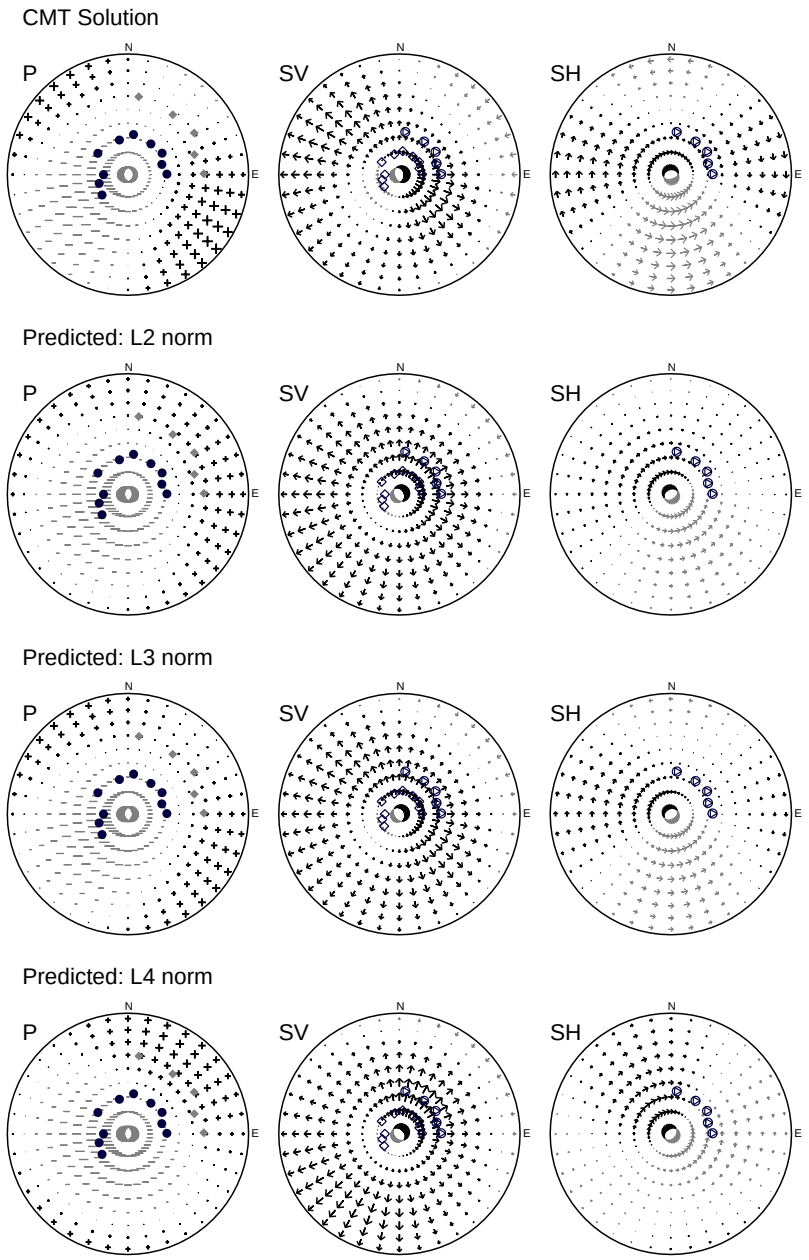

Fig. 5.11. Comparison of source radiation patterns for *P*, *SV* and *SH* waves obtained from inversion of the southern Xinjiang event using L_2, L_3 and L_4 norms. Also shown for comparison are the radiation patterns for the CMT solution. The plotted symbols represent the average take-off angle and azimuth for various phases; solid circles for *P*, solid triangles for *pP*, solid (grey) diamonds for *pS*; open circles for *S*, open triangles for *sS*, and open diamonds for *sP*.

Comparison of the predicted seismograms and source mechanisms obtained from inversion with different L_p norm misfit measures reveals noticeable differences. For example, inspection of the predicted seismograms obtained with a L_4 norm reveals that the inversion is trying to fit noise. A comparison between the observed and predicted

seismograms for a L_3 norm inversion is given in Figure 5.10. The use of a L_3 norm produces the best fitting *P* and *SV* waveforms out of the various L_p norms tested. The *SH* waveforms are not fit very well for any of the norms tested due to the poor quality of the waveforms. In Figure 5.11 we compare source radiation patterns for the CMT solution, with those obtained from inversion with L_2, L_3 and L_4 norm misfit measures. There are noticeable differences between the predicted source radiation patterns. The L_3 norm produces the closest fit to the source mechanism obtained from the CMT inversion, however the CMT solution is not necessarily the true solution.

Our investigations with different L_p norm misfit measures for this event have revealed that a L_3 norm measure gives the best results. Out of the various L_p norms tested, the L_3 norm gives the largest reduction in misfit. This misfit measure also produces the best fit between observed and predicted seismograms, and a source mechanism which closely matches the CMT mechanism. The L_3 norm is more sensitive to misfits in the seismograms than L_p norm measures with $p < 2$, and so provides stronger constraints. The L_4 norm measure is also sensitive to outliers but is affected by noise. The L_3 norm provides the best balance for this particular event, however this is not necessarily true for all events. A different L_p norm misfit measure might be better for other events, particularly if the noise characteristics differ.

5.3.4 Error analysis

It is often not very meaningful to take the best fitting model found within the specified number of iterations, as there may exist a number of models which satisfactorily fit the data. This is the case in the presence of non-uniqueness and noise. If noise is present in the data the best fit model will be determined by the noise, and there will exist a range of other data-acceptable models. In such cases an indication of the uncertainties associated with the best fitting model parameters can be obtained by examining the range of models which fit the data adequately. The NA is suited to such an approach as it can be geared to generate an ensemble of models with acceptable data fit, rather than seeking a single optimal model.

It is enlightening to plot the complete set of models generated during the NA inversion, as this contains information about the distribution of well fitting models in parameter space. We illustrate such an approach for the southern Xinjiang event, and perform an inversion using a double couple plus isotropic component source representation. We choose to represent the source mechanism in terms of fault plane parameters as this allows a simple interpretation when plotting the ensemble of models, however the same approach could be used with a moment tensor

Table 5.1. *Comparison between the best double couple CMT solution and the NA solution obtained with a double couple plus isotropic component source representation.*

	Depth (km)	Strike (°)	Dip (°)	Rake (°)
CMT (fault plane 1)	15.0	253	43	324
CMT (fault plane 2)	15.0	10	67	233
NA inversion	15.0	13	58	230

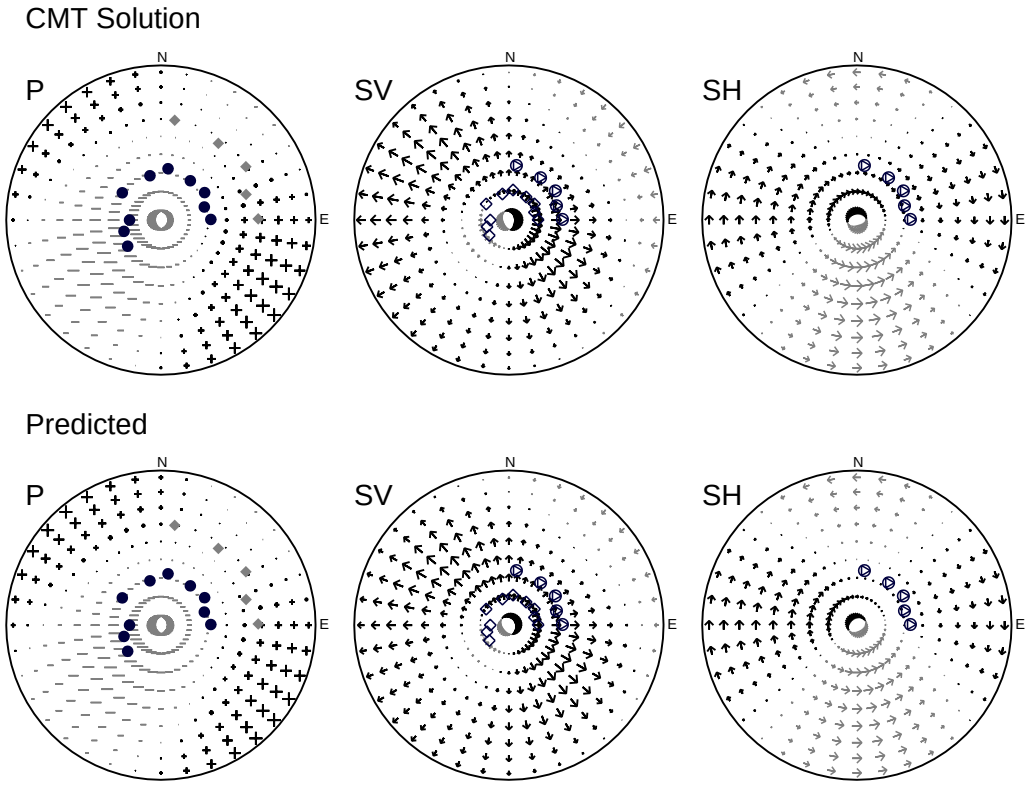

Fig. 5.12. Source radiation patterns for *P*, *SV* and *SH* waves for the southern Xinjiang event, using the CMT solution (top), and the predicted source mechanism obtained from the inversion with a double couple plus isotropic component source representation (bottom). The plotted symbols represent the average take-off angle and azimuth for various phases; solid circles for *P*, solid triangles for *pP*, solid (grey) diamonds for *pS*; open circles for *S*, open triangles for *sS*, and open diamonds for *sP*.

representation of the source. The best fitting model parameters found during the inversion give a misfit value of 0.162 and are displayed in Table 5.1, along with the best double couple solution found by the CMT inversion. The source depth and fault plane parameters obtained by the NA inversion closely match those of the CMT solution. We obtain a negligible isotropic weighting of 0.03, even though we do not apply any constraints to the allowable isotropic component. A comparison of the

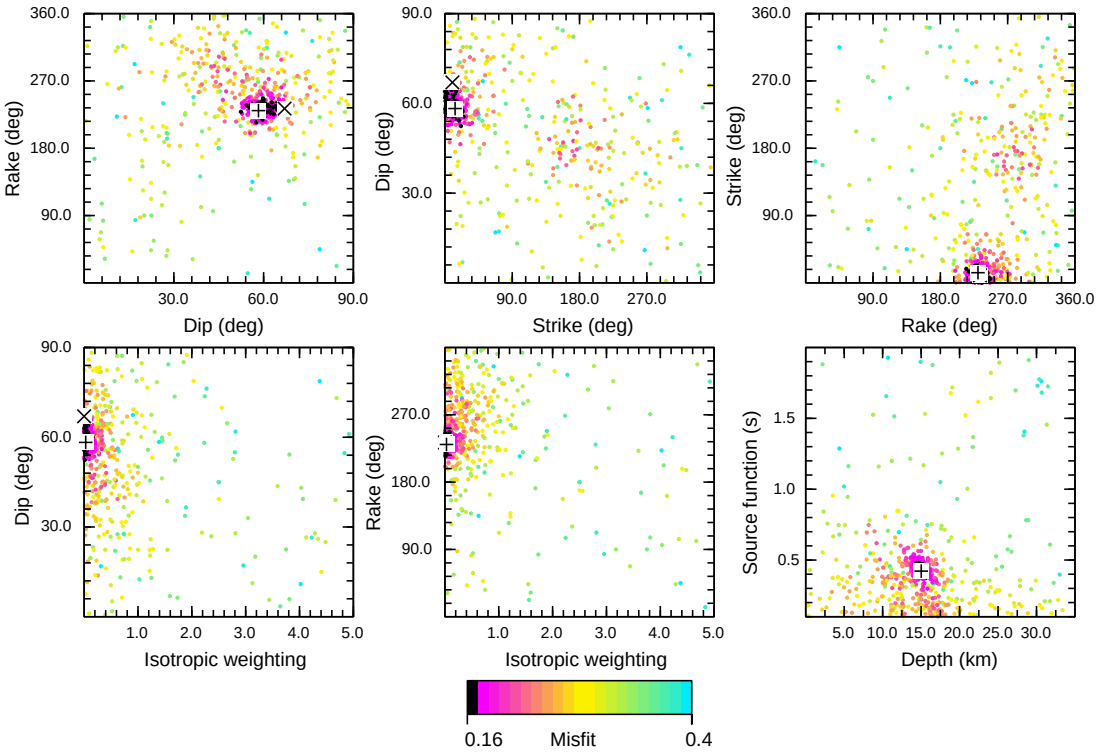

Fig. 5.13. Ensemble of models produced by the NA projected onto six pairs of parameter axes. Each plot range encompasses the entire parameter space. The best fit model is shown as a '+' and the CMT solution as a 'x'. The dots are coloured by misfit, as indicated by the scale.

source radiation patterns is provided in Figure 5.12, and we can see that the source mechanism estimates are very similar. Plotting the predicted seismograms reveals a good fit to the observed seismograms, similar to that obtained with a moment tensor inversion (see Figure 5.7).

Figure 5.13 displays the entire ensemble of models generated during the NA inversion with a double couple plus isotropic component source representation. Each plot represents the projection of the ensemble of models onto a two-dimensional plane. The colour scale represents misfit, with black representing models with a misfit value of less than 0.17. It is clear that the sampling is primarily concentrated in the regions of parameter space which have low misfit. These regions are fairly small and well defined, as would be expected given the good results obtained for this event. However, it is clear that there are regions of parameter space which are severely undersampled. There does not appear to be any evidence for the presence of local minima, though we might expect to see two minima in the fault plane parameters associated with the fault and auxiliary planes. There does seem to be some evidence for a trade-off between the

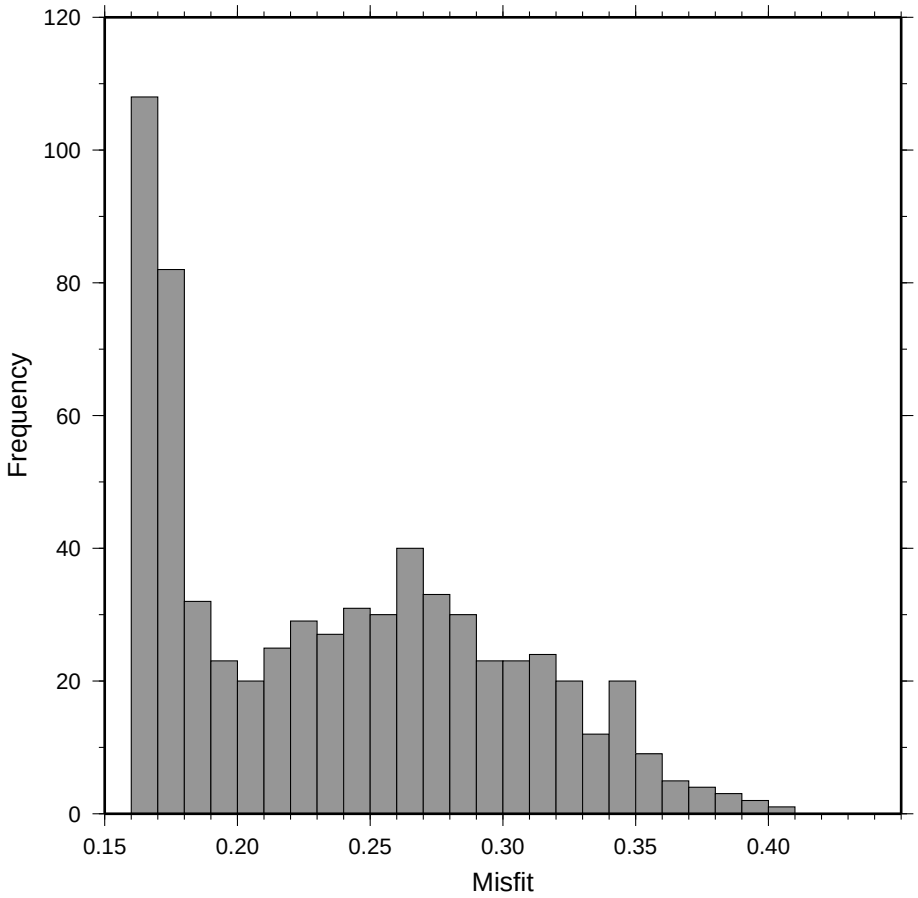

Fig. 5.14. Histogram of the misfit values for the 656 models produced during the NA inversion.

length of the source time function and depth, though this is not very clear due to the parameter space being undersampled. Such a trade-off occurs because a long source time function and a shallow source can produce similar looking waveforms as a shorter source time function and a deeper source. This trade-off has been observed by others (e.g., Stein and Kroeger, 1980, Christensen and Ruff, 1985), however, it generally does not produce major difficulties for small events.

Figure 5.14 shows a histogram of the misfit values associated with all the models generated during the NA inversion. We can see that the NA is doing a good job at exploring the parameter space by sampling areas with both high and low misfit. A large number of models (108 out of 656) have misfit values less than 0.17. Even though the sampling is primarily concentrated in the regions of parameter space which have low misfit, there is not enough information on the range of models which satisfactorily fit the data to be able to characterise the uncertainties associated with the best fitting model.